Geophysical Journal International

Geophys. J. Int. (2018) **212,** 942–954
Advance Access publication 2017 October 25
GJI Seismology

doi: 10.1093/gji/ggx465

Seismicity induced by longwall coal mining at the Thoresby Colliery, Nottinghamshire, U.K.

James P. Verdon,[1] J-Michael Kendall,[1] Antony Butcher,[1] Richard Luckett[2] and Brian J. Baptie[2]

[1]*School of Earth Sciences, University of Bristol, Wills Memorial Building, Queen's Road, Bristol* BS8 1RJ, *United Kingdom.*
E-mail: James.Verdon@bristol.ac.uk
[2]*British Geological Survey, The Lyell Centre, Research Avenue South, Edinburgh* EH14 4AP, *United Kingdom*

Accepted 2017 October 24. Received 2017 October 20; in original form 2017 July 12

SUMMARY

The United Kingdom has a long history of deep coal mining, and numerous cases of mining-induced seismicity have been recorded over the past 50 yr. In this study, we examine seismicity induced by longwall mining at one of the United Kingdom's last deep coal mines, the Thoresby Colliery, Nottinghamshire. After public reports of felt seismicity in late 2013 a local seismic monitoring network was installed at this site, which provided monitoring from February to October 2014. This array recorded 305 seismic events, which form the basis of our analysis.

Event locations were found to closely track the position of the mining face within the Deep Soft Seam, with most events occurring up to 300 m ahead of the face position. This indicates that the seismicity is being directly induced by the mining, as opposed to being caused by activation of pre-existing tectonic features by stress transfer. However, we do not observe correlation between the rate of excavation and the rate of seismicity, and only a small portion of the overall deformation is being released as seismic energy.

Event magnitudes do not follow the expected Gutenberg–Richter distribution. Instead, the observed magnitude distributions can be reproduced if a truncated power-law distribution is used to simulate the rupture areas. The best-fitting maximum rupture areas correspond to the distances between the Deep Soft Seam and the seams that over- and underlie it, which have both previously been excavated. Our inference is that the presence of a rubble-filled void (or goaf) where these seams have been removed is preventing the growth of larger rupture areas.

Source mechanism analysis reveals that most events consist of dip-slip motion along near-vertical planes that strike parallel to the orientation of the mining face. These mechanisms are consistent with the expected deformation that would occur as a longwall panel advances, with the under- and overburdens moving upwards and downwards respectively to fill the void created by mining. This further reinforces our conclusion that the events are directly induced by the mining process. Similar mechanisms have been observed during longwall mining at other sites.

Key words: Geomechanics; Earthquake source observations; Induced seismicity; Seismic anisotropy.

1 INTRODUCTION

Seismicity induced by coal mining has been a common occurrence in the United Kingdom (e.g. Redmayne 1988). Indeed, Wilson *et al.* (2015) estimated that between 20 and 30 per cent of all earthquakes recorded in the United Kingdom between 1970 and 2012 were induced by coal mining. From the late 1980s onwards the rate of coal production has declined significantly, as has the rate of associated earthquakes (Fig. 1).

Nevertheless, seismicity associated with deep coal mining still occurs in the United Kingdom. Between December 2013 and January 2014, the United Kingdom's national seismometer network detected a series of over 40 earthquakes near to the village of New Ollerton, Nottinghamshire. The largest of these events had a magnitude of $M_L = 1.7$. Given the generally low levels of seismicity in the United Kingdom, the village was dubbed the 'United Kingdom's Earthquake Capital' (Turvill 2014). The area has a history of seismic activity relating to coal mining (e.g. Bishop *et al.* 1993), and it was soon identified that the events were likely to be associated with longwall coal mining at the nearby Thoresby Colliery, which at the time was one of the few remaining deep coal mining sites in the United Kingdom.

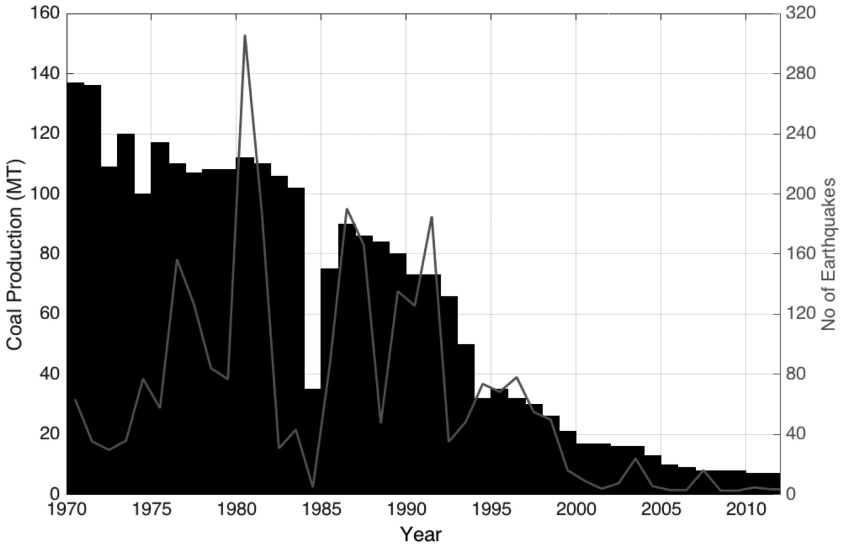

Figure 1. Deep mined coal production in the United Kingdom by year (bars) and the number of induced earthquakes per year associated with coal mining (grey line), as categorised by Wilson *et al*. (2015). The drop in both production and induced seismicity in 1984 is associated with the U.K. miner's strike.

In response to the felt earthquakes, a temporary local monitoring network of surface seismometers was deployed between the 5th February and the October 30th, 2014 by the British Geological Survey (BGS). This network recorded a further 300 seismic events. The high quality of the data recorded by the local network permits a detailed study into the nature of seismicity and deformation induced by the longwall mining process.

1.1 Longwall coal mining at Thoresby

The Thoresby Colliery opened in 1925. Over the history of the site, at least four different seams have been mined, including the High Hazels, Top Hard, Deep Soft and Parkgate Seams, in order from shallowest to deepest: see Edwards (1967) for a stratigraphic section showing the positions of these and other seams in the region. The Deep Soft Seam was the last to be developed, with work beginning in 2010: this was the only seam being actively mined during the study period. The colliery closed entirely in mid-2015. This was for economic reasons related to the low price of coal, not because of the induced seismicity.

The Deep Soft Seam was mined using standard longwall methods: hydraulic jacks are used to support the roof while a shearing device cuts coal from the face. As the face advances, the jacks are moved forward, allowing the roof to collapse into the cavity that is left behind. The collapsed, brecciated roof material filling this void is known as goaf (e.g. Younger 2016). At Thoresby, each longwall panel has dimensions of approximately 300 m width, between 1000 and 3000 m length, and approximately 2.5 m height.

1.2 Seismicity associated with longwall coal mining

Seismicity has often been associated with the longwall mining process (e.g. Cook 1976; Gibowicz *et al*. 1990; Bishop *et al*. 1993; Stec 2007; Bischoff *et al*. 2010; Sen *et al*. 2013). Seismic events associated with coal mining have often been divided into two categories: 'mining-tectonic' activity, produced by activation of pre-existing tectonic faults, and 'mining-induced' activity, directly associated with the mining excavations (e.g. Stec 2007).

Observed magnitudes have typically ranged from $0.5 < M_L < 3.5$. At some sites event magnitudes have followed the Gutenberg & Richter (1944) distribution (e.g. Bishop *et al*. 1993; Kwiatek *et al*. 2011), while in other cases bimodal or other frequency–magnitude distributions have been observed (e.g. Stec 2007; Hudyma *et al*. 2008; Bischoff *et al*. 2010). These non-Gutenberg–Richter distributions have been attributed to the presence of characteristic length scales (the dimensions of the mined panels, for example) that provide a control on rupture dimensions and thereby event magnitudes.

Analysis of event focal spheres has revealed a variety of source mechanisms in different settings (e.g. Stec 2007; Bischoff *et al*. 2010; Sen *et al*. 2013) including: non-double-couple events, indicating a volumetric component of deformation usually associated with the roof collapse process; double-couple events showing a direct relationship to mined panels, with vertical fault planes running parallel to the mining face, on which dip-slip motion occurs; and double-couple events that correspond to regional fault orientations and *in situ* tectonic stress conditions.

In this paper we follow the processes developed in the aforementioned studies to characterize the seismicity induced by mining at the Thorseby Colliery. We begin by locating events, comparing the event locations to the propagation of the mining faces with time, and seismicity rates with the volume of coal extracted from the mine. We investigate the source characteristics of the events, using spectral analysis combined with event frequency–magnitude distributions to assess the length-scales of structures that have generated the observed events. We use shear-wave splitting analysis to image *in situ* stress orientations at the site, and we calculate focal mechanisms for the events to establish the orientations of fault planes and slip directions generated by the mining process.

2 EVENT DETECTION AND LOCATION

2.1 Monitoring array and event detection

The local surface network deployed to monitor seismicity at the Thoresby Colliery comprised of 4 3-component Guralp 3ESP broad-band seismometers (stations NOLA, NOLD, NOLE and NOLF) and 3 vertical-component Geotech Instruments S13J short-period seismometers (NOLB, NOLC and NOLG)). The station positions are shown in Fig. 2. Events were detected using the BGS's in-house event detection algorithm, which is based on

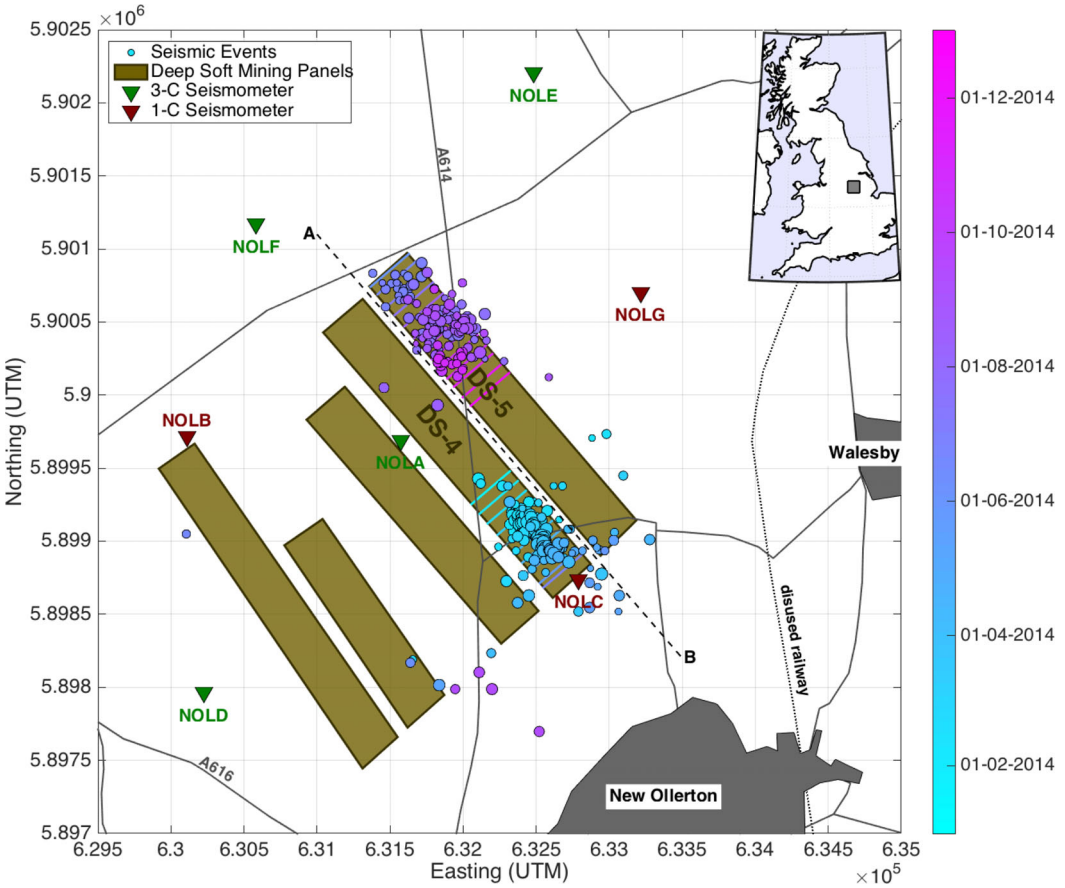

Figure 2. Map of event hypocentres, with events coloured by occurrence date. Also shown are the positions of the monitoring network (triangles) and the mining panels (brown rectangles). Panels DS-4 and DS-5 were active during the monitoring period, and the coloured bars running across these panels show the forward movement of the mining faces with time. The position of the cross-section A–B (Fig. 5) is marked by the dashed line.

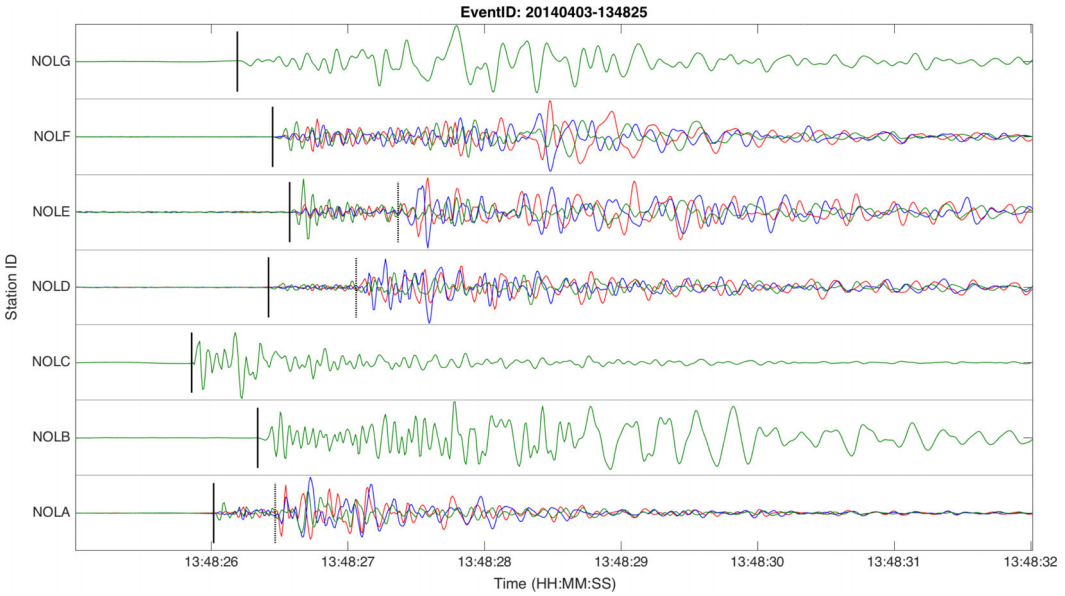

Figure 3. Recorded waveforms for a larger event ($M_L = 1.3$). The N (red), E (blue) and Z (green) components for each station are overlain. Stations NOLB, NOLC and NOLG are single (Z) component stations. The *P*- and *S*-wave picks are marked by the solid and dashed tick marks.

identification of peaks in running short-time/long-time averages (STA/LTA), as described by Allen (1982). A total of 305 events were identified during the deployment of the local monitoring network.

P- and *S*-wave arrival times were repicked manually for every event (e.g. Fig. 3). For most event-station pairs the *P*-wave arrival was clear and unambiguous, and so could be accurately picked (83 per cent of station-event pairs where a pick could be manually

Table 1. 1D, layered, isotropic velocity model used to locate events. Model is based on that used by Bishop *et al*. (1993).

Layer no.	Depth to layer top (m)	V_P (ms^{-1})	V_S (ms^{-1})
1	0	1900	1280
2	60	2750	1540
3	135	3100	1740
4	275	3500	1970
5	1019	4200	2360
6	1351	5250	2920
7	2751	6000	3370

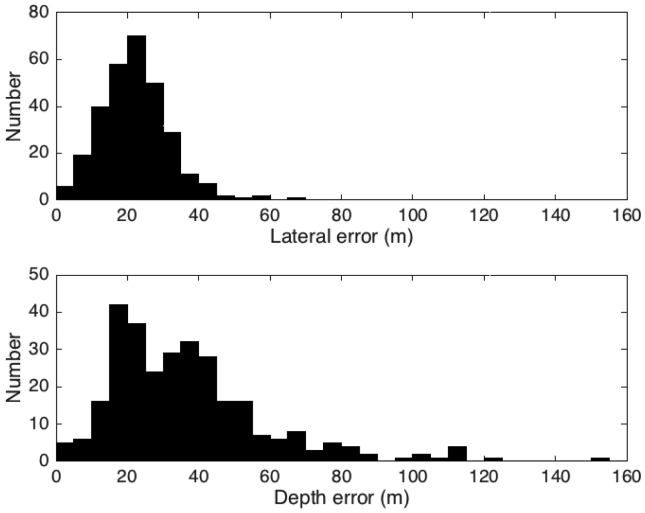

Figure 4. Histograms showing the lateral and depth uncertainties for the located events.

assigned). Stations NOLB, NOLC and NOLG were single, vertical component stations, so *S*-wave picks were not made for these stations. For smaller events with lower signal-to-noise ratios, clear *S*-wave arrivals were sometimes difficult to identify, resulting in a lower number of picks (74 per cent of station-event pairs where a pick could be manually assigned).

The velocity model used to locate the events is taken from Bishop *et al*. (1993), and is listed in Table 1. The arrival time picks were inverted for the best-fitting location that minimizes the least-squares residual between modelled and picked arrival times. The search for the best-fitting location was performed using the Neighbourhood Algorithm (Sambridge 1999), and the modelled travel times were calculated using an eikonal solver (Podvin & Lecomte 1991). A map of event hypocentres is shown in Fig. 2, in which the mining panels and the position of the mining face with time are also shown.

In Fig. 4 we show histograms of the event location uncertainties laterally and in depth. Note that these uncertainties pertain solely to the residuals between picked and modelled arrival times, and do not account for velocity model uncertainties. The velocity model used is based on limited site-specific data, relying mainly on regional seismic refraction surveys (Bishop *et al*. 1993).

A brief sensitivity analysis suggested that velocity model uncertainties of up to 10 per cent may affect depth locations by as much as 150 m, while lateral locations are relatively unaffected. This reflects the geometry of the array, which provides reasonable azimuthal coverage but with surface stations only, such that an uncertain velocity model will primarily affect the event depths.

Fig. 5 shows a cross-section of event depths relative to the coal seams. We note that, while it appears that the events are located below the seam depths, given the likely velocity model uncertainties; it is not possible to rule out that these events are actually located at the same depths as the Deep Soft Seam being mined.

2.2 Event locations with respect to mining activities

The positions of the mining panels, and the progress of the mining face with time, have been provided by the UK Coal Authority in their Mine Abandonment Plans (2017). The position of the mining face with respect to the events can be seen in Fig. 2. It is immediately

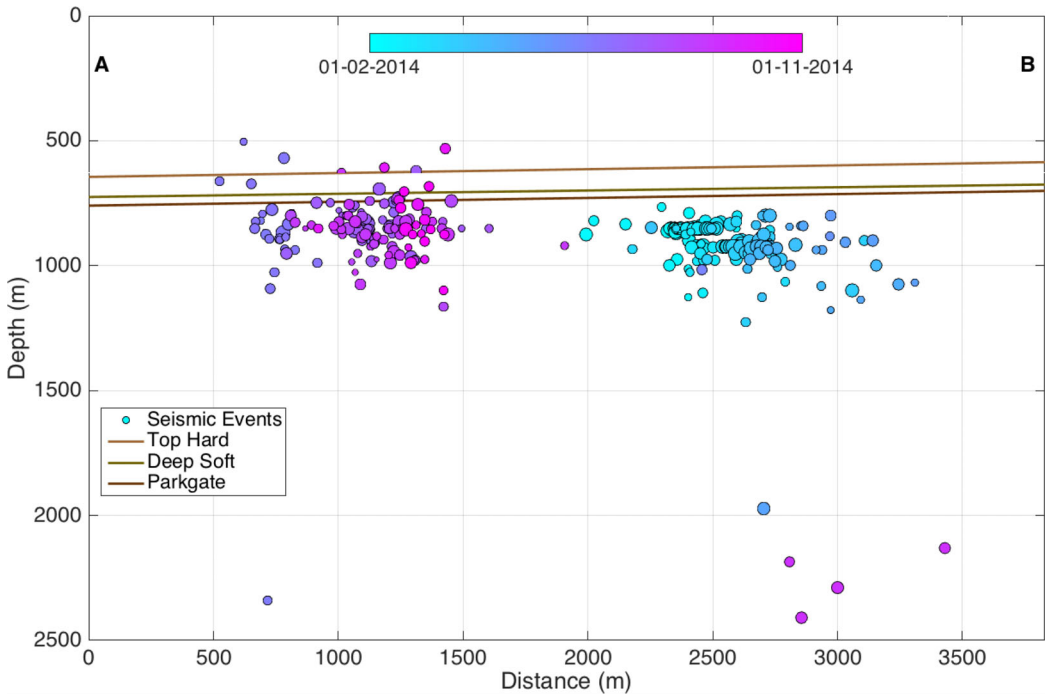

Figure 5. Events depths shown along cross-section A–B (see Fig. 2). The positions of the Top Hard, Deep Soft and Parkgate Seams are also marked. Note that velocity uncertainties mean that the event depths may not be particularly well constrained.

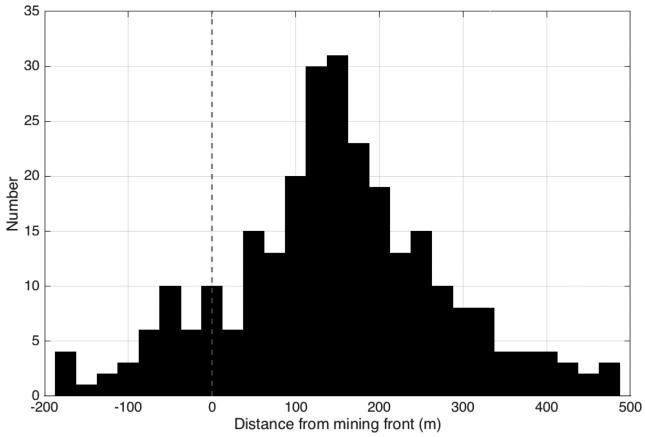

Figure 6. Histograms showing the lateral position of each event relative to the mining face at the time of event occurrence, where a positive distance represents events occurring in advance of the face.

apparent that the event locations are tracking the position of the face as it moves SE along panel DS-4, before switching to DS-5 and again tracking the mining front to the SE. The monitoring period ceases when the events have propagated approximately half-way along the length of panel DS-5.

We investigate the position of events in relation to the mining face in greater detail in Fig. 6, which shows a histogram of event positions relative to the mining face, along an axis parallel to the mining panels. Most events are found to occur ahead of the face, with most events occurring within 300 m of the face. This close correlation between events and the mining face implies that the events are being directly induced by mining activities, as opposed to the activation of pre-existing tectonic features, in which case we would expect the events to align along an activated fault. As per the categorisation described by Stec (2007), we characterise these as mining-induced events.

However, we also note small cluster of five events that is found at greater depths (>2000 m), to the SW of the DS-4 panel. Four of these five events occurred within a single 7-hr period. Establishing the causality of these events is more difficult. It is possible that these events have been have been triggered by the static transfer of stress changes to greater depths, leading to fault activation. As per the Stec (2007) categorisation, these may be mining-tectonic events. However, it is not possible to rule out that these deeper events may in fact have a natural origin.

3 CORRELATION BETWEEN SEISMICITY AND MINING RATES?

In Fig. 7 we show the volume of rock removed from the mine on a weekly basis (ΔV), the number of events per week (N_E), and the cumulative seismic moment ($\sum M_O$) released per week. The volume of rock removed per week is estimated from the forward progress of the mining face, multiplied by its dimensions (width and height). To further investigate any correlation between the extracted volume and seismicity, in Fig. 8 we cross-plot these parameters. From Fig. 8 it is apparent that there is little immediate correlation between ΔV and N_E and $\sum M_O$ on a weekly basis.

McGarr (1976) posited a linear relationship between ΔV and $\sum M_O$:

$$\Sigma M_O \approx \mu \Delta V, \tag{1}$$

where μ is the rock shear modulus. This relationship corresponds to the situation whereby all of the deformation produced by the volume change is released seismically. In reality, much of the deformation may occur aseismically. As such, Hallo *et al*. (2014) proposed a modification to this relationship via a 'seismic efficiency' term, S_{EFF}, which describes the portion of the overall deformation that is released as seismic energy:

$$\Sigma M_O \approx S_{EFF} \mu \Delta V. \tag{2}$$

In some of the most well-known cases of induced seismicity, values of S_{EFF} have been close to 1 (e.g. McGarr 2014). However, these cases represent outliers: during most industrial operations S_{EFF} is much less that 1 (e.g. Hallo *et al*. 2014). The dashed lines in Fig. 8(b) show the relationship between ΔV, $\sum M_O$ and S_{EFF}, assuming a generic value of $\mu = 20$ GPa. We note that the observed moment release rates correspond to values of S_{EFF} between 0.01 and 0.00001, implying that most of the deformation induced by the mining is released aseismically. This is typical for many cases of seismicity induced by a variety of industrial activities (e.g. Maxwell *et al*. 2008; Hallo *et al*. 2014).

4 EVENT MAGNITUDES AND FREQUENCY–MAGNITUDE DISTRIBUTIONS

4.1 Moment magnitude calculation

Local magnitudes for the Thoresby Colliery seismicity have been computed by Butcher *et al*. (2017), who found that the United Kingdom's existing local magnitude scale (Ottemöller & Sargeant 2013)

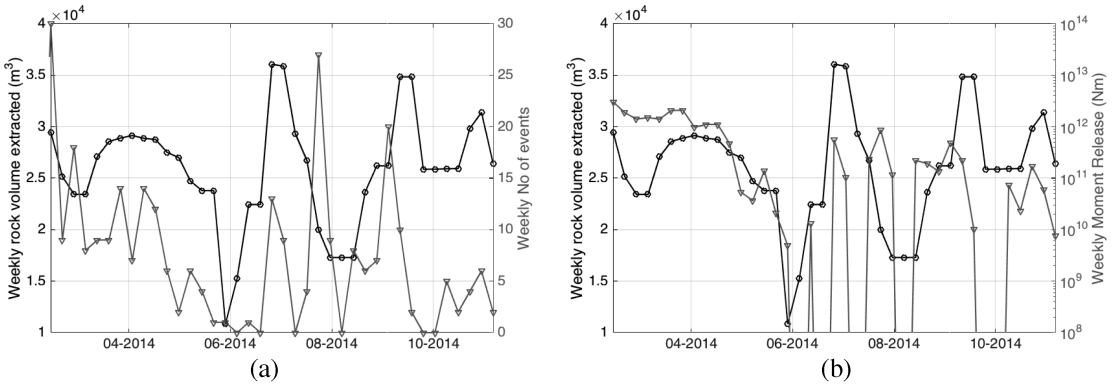

Figure 7. Weekly rock volume extracted (black lines) compared with (a) the weekly number of recorded events and (b) the weekly cumulative seismic moment released (grey lines).

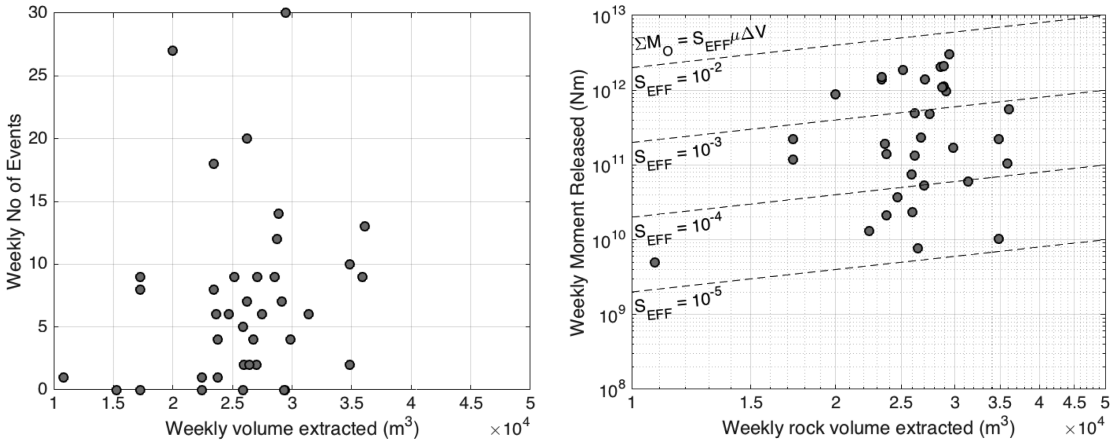

Figure 8. Cross-plots examining potential correlation between weekly rock volume extracted and the weekly number of recorded events (a) and the weekly cumulative seismic moment released (b). In (b), the dashed lines show the expected relationship for given values of S_{EFF}.

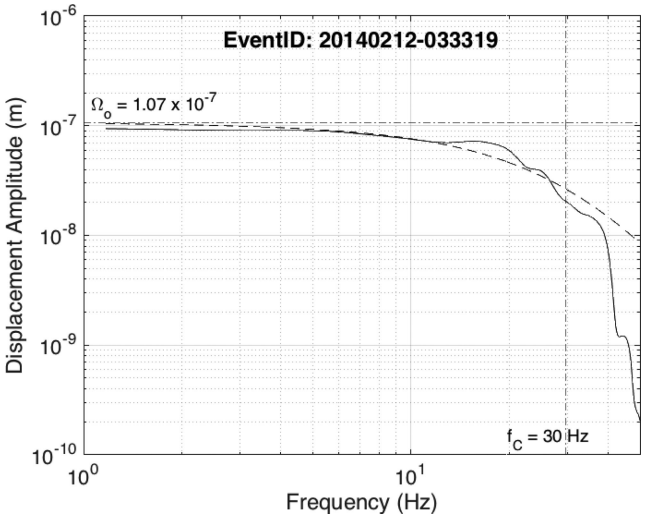

Figure 9. Example displacement spectrum used to estimate moment magnitudes. The solid line shows the observed spectrum, while the dashed line shows the best-fitting Brune (1970) source model. The dot–dashed lines show the f_{C} and Ω_{O} values for this model.

is not appropriate for use when sources and receivers are within a few kilometres of each other. This is because for nearby receivers, the ray path will be predominantly through the softer, more attenuative sedimentary cover, rather than the underlying crystalline crustal rocks, as will be the case for receivers that are more distant to the event. Butcher *et al*. (2017) have developed an alternative local magnitude scale based on the Thoresby events, which has been re-calibrated to ensure consistency between magnitude measurements made on nearby stations and those made using the UK's permanent national monitoring network, the nearest stations of which were some distance from the Thoresby site.

However, our aim here is to investigate event magnitude distributions in order to understand the length scales of structures being affected by the mining process. This therefore requires the use of moment magnitudes, since seismic moment can be directly related to rupture dimensions. We compute moment magnitudes by fitting a Brune (1970) source model to the observed *S*-wave displacement amplitude spectra (Fig. 9), following the method described by Stork *et al*. (2014). The seismic moment is determined from the amplitude of the low-frequency plateau, Ω_{O}.

Ideally, the measured corner frequency, f_{C}, of the displacement spectra could be used to determine the rupture length. However, to robustly image the corner frequency, it must be significantly lower than the Nyquist frequency, f_{N} of the recording system—Stork *et al*. (2014) recommend that $f_{\mathrm{N}} > 4f_{\mathrm{C}}$ to obtain robust estimates of f_{C}. The recording systems at Thoresby had sampling rates of 100 Hz, so $f_{\mathrm{N}} = 50$ Hz.

We can use generic values for stress drop and rupture lengths to establish the expected corner frequencies for events with $M_{\mathrm{W}} < 1$. Using the relationships between rupture dimensions, seismic moment and stress drop given by Kanamori & Brodsky (2004), assuming a stress drop of 5 MPa and a rupture velocity of 2000 m s^{-1}, the resulting corner frequency $f_{\mathrm{C}} \approx 30$ Hz. Evidently, the $f_{\mathrm{N}} > 4f_{\mathrm{C}}$ criteria is not expected to hold for this particular dataset. However, our observations of event magnitudes, because they are derived from the amplitude spectra at low frequencies, are robust: we therefore use these to make inferences about the length scales of the structures that have generated the observed seismic events.

4.2 Frequency–magnitude distributions

The observed event magnitude distribution (EMD) is shown in Fig. 10. We show the EMDs for the overall dataset, as well as individually for the clusters associated with the DS-4 and DS-5 panels. The overall dataset is not well described by the Gutenberg & Richter (1944) distribution $\log_{10} N\,(M) = a - bM$, where $N(M)$ is the cumulative number of events larger than a given magnitude M, and a and b are constants to be determined. Such a distribution would be represented by a straight line in M versus $\log_{10}(N)$ space. We note that the apparent limit on the largest event size is not an artefact of a short measuring period: while the local array was removed in October 2014, the area continues to be monitored by the BGS National Seismometer Array, which has an estimated detection capability across the United Kingdom of magnitude >2. Larger events occurring after the study period would therefore be detectable, but no such events have occurred.

However, fault length and/or earthquake magnitude distributions that are constrained at some upper limit, leading to a fall-off from the power-law (PL) relationship at large values, have been suggested by a number of authors. At the largest scale, Richter (1958) argues that 'a physical upper limit to the largest possible magnitude must be set by the strength of crustal rocks, in terms of the maximum

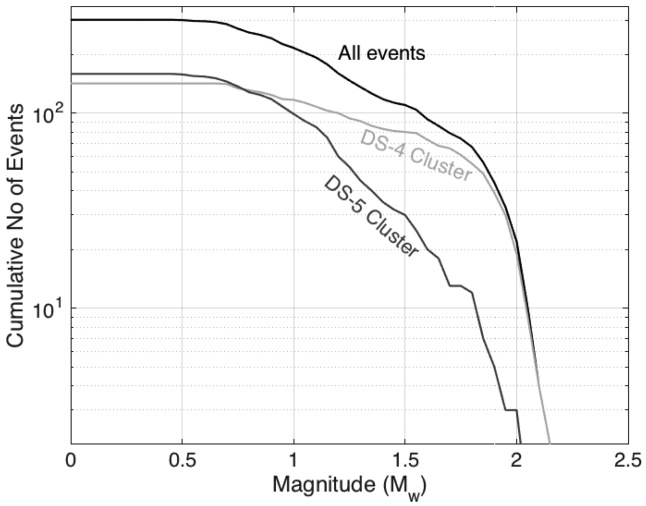

Figure 10. Observed frequency-magnitude distributions for the full event population (black), as well as for the DS-4 (light grey) and DS-5 (dark grey) clusters individually.

Table 2. Best-fitting power law and truncated power-law distributions for each of the DS-4 and DS-5 clusters, and the resulting normalised misfits.

	Dist. Type	α	C	A_{MAX}	Misfit
DS-4	PL	0.47	1707	NA	5.46
	TPL	0.1	743	10075	1.23
DS-5	PL	0.74	6861	NA	3.05
	TPL	0.38	1536	3870	0.86

strain which they are competent to support without yielding'. Similarly, Pacheco *et al*. (1992) argue that the rupture dimensions of very large earthquakes are limited by the thickness of the Earth's seismogenic zone (the portion of the crust that is capable of undergoing brittle failure). For continental rift zones, Scholz & Contreras (1998) suggested that the maximum length of normal faults would be limited by the flexural restoring stress and friction, and found a good match between their model and faults in the East African Rift and in Nevada. At a much smaller scale, Shapiro *et al*. (2013) have suggested these effects will also apply to induced seismicity, with the maximum fault size, and therefore earthquake magnitude, determined by the dimensions of the volume stimulated by human activities.

To understand the observed EMDs at Thoresby, we consider the statistical distributions of fault rupture areas that might produce them. Typically, rupture areas are assumed to follow a self-similar, PL distribution (e.g. Wesnousky *et al*. 1983; Bonnet *et al*. 2001). If stress drops are assumed to be roughly constant (e.g. Abercrombie 1995) then this PL rupture area distribution will result in a PL distribution of magnitudes, that is the Gutenberg–Richter distribution.

A cumulative PL distribution for rupture area will take the form:

$$N(L) = CA^{-\alpha}, \tag{3}$$

where $N(A)$ is the number of ruptures with area greater than length A, α is the PL exponent, and C is a constant. For a PL distribution, there is no upper limit to the maximum rupture area. Instead, if an upper limit to the rupture area is imposed, for example by the geometry of the mining panels, then a truncated power-law (TPL) distribution results (Burroughs & Tebbens 2001, 2002):

$$N(A) = C\left(A^{-\alpha} - {A_{\mathrm{MAX}}}^{-\alpha}\right), \tag{4}$$

where A_{MAX} is the maximum rupture area.

To simulate event magnitudes based on rupture area, we use Kanamori & Brodsky (2004):

$$M_{\mathrm{O}} = \Delta\sigma A^{3/2}, \tag{5}$$

where $\Delta\sigma$ is the stress drop. As discussed above, the limitation of a relatively low Nyquist frequency means that we cannot measure the stress drop directly. Therefore, to estimate the PL and TPL parameters that best-fitting our observations, we initially assume a generic and arbitrary stress drop of $\Delta\sigma = 5$ MPa.

For each of the DS-4 and DS-5 event clusters, we perform a search over the PL and TPL parameters, finding those that minimise the least-squares misfit between observed and modelled EMDs. The resulting EMDs are shown as the solid lines in Fig. 11, with the PL and TPL parameters, and the misfit for each of the models, listed in Table 2. The resulting rupture area distributions are shown in Fig. 12.

Having established the best-fitting PL and TPL distributions with a fixed stress drop value, we then investigate the impact of a variable range of $\Delta\sigma$. We do this in a stochastic manner, simulating rupture area distributions based on the PL and TPL parameters, assigning stress drops randomly from a uniform distribution of

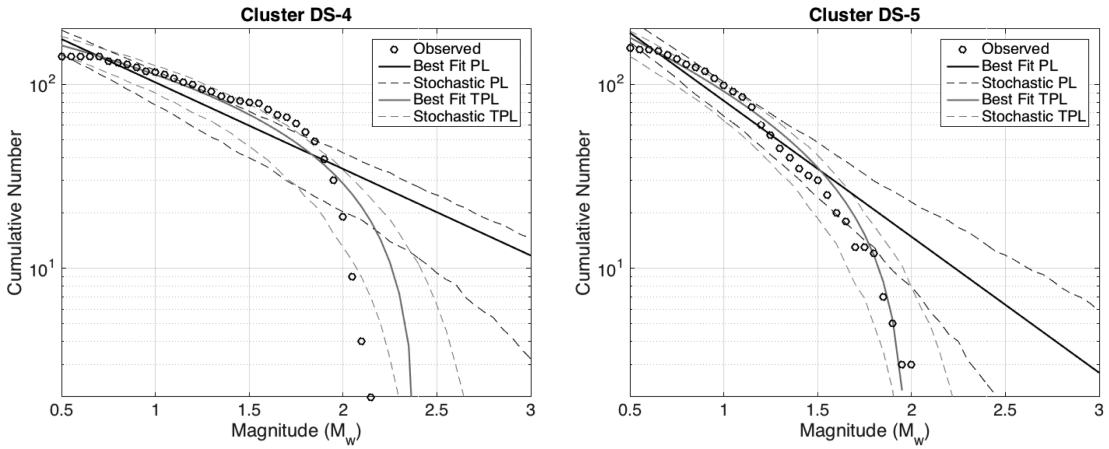

Figure 11. Fitting PL (black) and TPL (grey) rupture area distributions to the DS-4 (a) and DS-5 (b) EMDs. Observed EMDs are shown by black circles. The solid lines show the best-fitting models for a fixed $\Delta\sigma$ value, while the dashed lines show ± 2 standard deviations when $\Delta\sigma$ is varied stochastically.

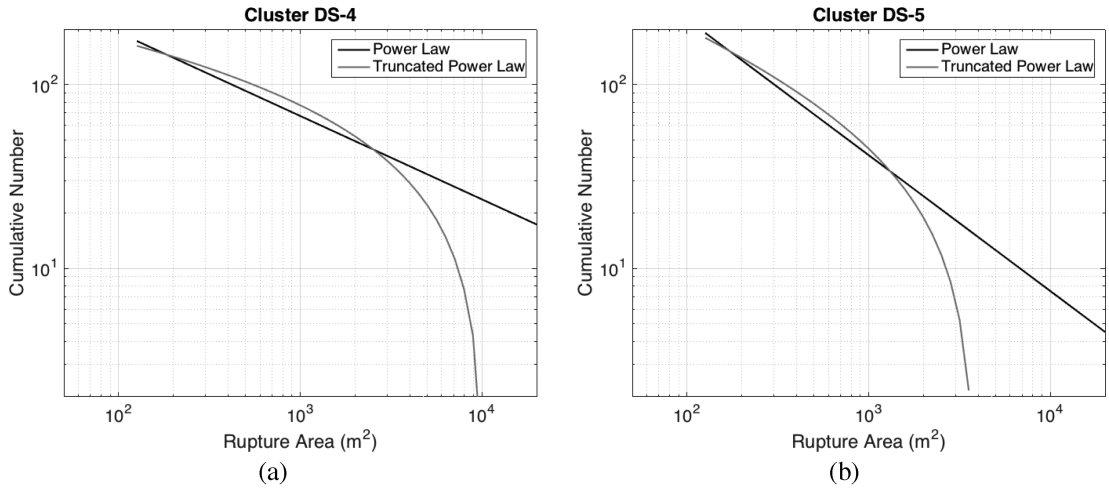

Figure 12. Best-fitting rupture area PL (black) and TPL (grey) distributions for the DS-4 (a) and DS-5 (b) clusters.

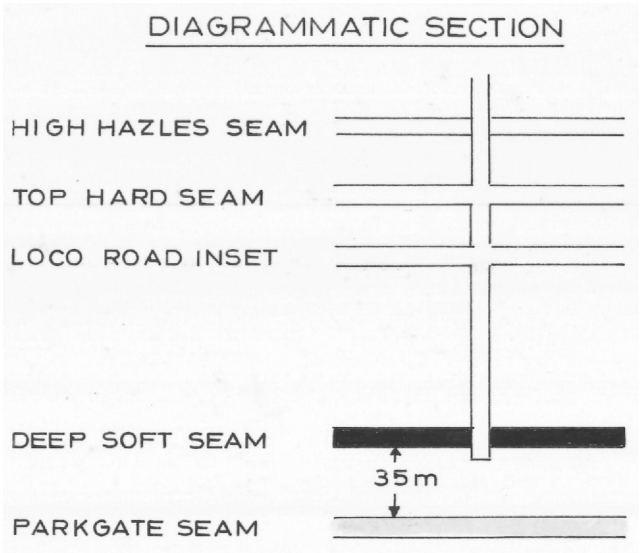

Figure 13. Diagrammatic section showing the spacing between the Deep Soft Seam, and the underlying Parkgate Seam, which has already been mined out across the study area. Image taken from UK Coal Authority Mine Abandonment Plans (2017).

$0.1 < \Delta\sigma < 20$ MPa. We repeat this process over 100 iterations, and in Fig. 11 the dashed lines show the range encompassing ± 2 standard deviations around the resulting mean EMD. From Fig. 11 we observe that both event populations are clearly better modelled by a TPL rupture area distribution, even when stochastic variation in $\Delta\sigma$ is considered.

Based on these results, it is worth examining whether the best-fitting values for A_{MAX} correspond to any length-scales associated with the mining activities. There are two length scales in play that might affect rupture dimensions: the width of the mining face (approximately 300 m); and the separations between (1) the underlying Parkgate Seam, which is 35 m below the Deep Soft (Fig. 13), and (2) the overlying Top Hard Seam, which is approximately 110 m above the Deep Soft. Both seams have already been mined throughout our study area. The voids left by the longwall mining of these seams will be filled with goaf, the rubble and detritus created as the roof collapses behind the mining face. It is difficult to envisage a mechanism by which ruptures could propagate through such a rubble-filled void.

Assuming circular ruptures, areas of 10 075 and 3870 m^2 correspond to rupture radii of 57 and 35 m. The larger dimension radius is therefore roughly equivalent to a circular rupture extending from the Deep Soft to the Top Hard. Alternatively, assuming a rectangular rupture, the DS-4 A_{MAX} value could correspond to a rupture with dimensions of approximately 35 $\times$ 300 m, equivalent to a rupture extending from the Deep Soft to the Parkgate, across the length of the mined face. In reality, ruptures will not be rectangular nor circular. Nevertheless, the general agreement between the dimensions of the maximum rupture area and these distances leads us to suggest that the presence of the overlying and underlying Top Hard and Parkgate seams is indeed limiting the rupture dimensions. Given the similarities between these dimensions, it is not possible to determine whether one of these features in particular is controlling the maximum rupture area. Indeed, it is likely that all three features: the width of the mining face; the distance to the underlying Parkgate Seam; and the distance to the overlying Top Hard Seam, are all playing a role in limiting the maximum rupture dimensions.

5 SEISMIC ANISOTROPY AND SHEAR-WAVE SPLITTING

Shallow crustal anisotropy can be generated by several mechanisms, including: alignment of macroscopic fracture networks; the preferential alignment of microcracks due to anisotropic stress field (in practice, the microscopic and macroscopic effects often combine, as both larger-scale fracture networks and microcracks are preferentially opened or closed by the same stress field); and by the alignment of sedimentary bedding planes.

Shear-wave splitting (SWS), where the velocity of a shear-wave is dependent upon the direction of travel and the polarity of the wave, is an unambiguous indicator of seismic anisotropy, and has been used previously to image stress changes induced by mining activities (Wuestefeld *et al*. 2011). Shear waves that propagate near-vertically will not be sensitive to horizontally layered sedimentary fabrics, which produce Vertically Transverse-Isotropy (VTI) symmetry systems. Instead, in the absence of other major structural fabrics, the fast shear wave polarisation orientation can be treated as a proxy for the direction of maximum horizontal stress (e.g. Boness & Zoback 2006).

We perform SWS measurements on the Thoresby data. Accurate SWS measurements can only be obtained within the '*S*-wave window' (Crampin & Peacock 2008), because arrivals at an incidence

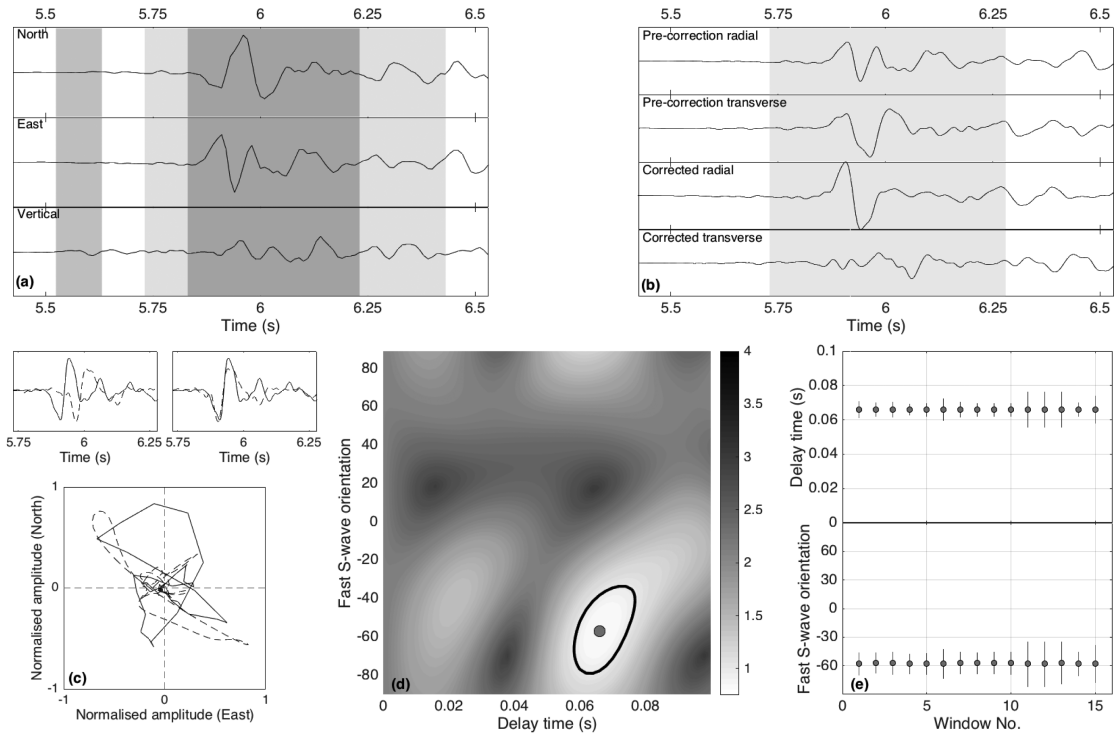

Figure 14. Example shear-wave splitting measurement using the method described by Teanby *et al*. (2004). In (a) we plot the N, E and Z components of the recorded waveforms, where *P*- and *S*-wave windows are highlighted by the shaded areas. In (b) we plot the radial and transverse components prior to and after the splitting correction, where the aim of the correction is to minimise energy on the transverse component. In (c) we plot the waveform particle motions before (solid lines) and after (dashed lines) correction. In (d) we plot the error surfaces of the correction method as a function of delay time and fast direction normalised such that the 95 per cent confidence interval (highlighted in bold) is 1. In (e) we plot the best-fitting delay times and fast directions that result from choosing different *S*-wave window start and end times [as indicated by the light-grey shaded zone of (a)].

angle greater than ∼35° from vertical may be disturbed by *S*-to-*P* conversions at the free surface. This constraint limits the available data considerably, such that events within the *S*-wave window are found only on station NOLA, and for only 28 of the recorded events.

We perform the SWS measurement using the automated cluster-based approach described by Teanby *et al*. (2004). Where larger datasets are studied, automated quality assessments such as that described by Wuestefeld *et al*. (2010) can be used, but in this case, given the small sample size, the quality of measurements were assessed manually. Of the 28 arrivals within the *S*-wave window at NOLA, 9 provided good-quality, robust results according to the diagnostic criteria specified by Teanby *et al*. (2004). This is a typical rate-of-return for such studies given the relatively low magnitude (and therefore signal-to-noise) of the events. An example of a robust SWS measurement is provided in Fig. 14.

In Fig. 15(a) we show the measured fast directions in the form of an angle histogram. A dominant fast direction striking NW–SE is clearly observed. The mean fast direction azimuth is 130°. No temporal variations in SWS fast directions or percentage anisotropy were observed. The mean delay time was 43 ms, and the mean percentage *S*-wave anisotropy was 6.8 per cent.

In Fig. 15(b) we compare the measured fast *S*-wave orientations with independent measurements for S_{Hmax} taken from the World Stress Map database (Heidbach *et al*. 2008). These measurements, mainly from borehole breakouts and hydraulic fracturing tests, also indicate an approximate regional S_{Hmax} strike that is to the NW–SE. We conclude that the mean measured S-wave fast polarity of 130° can be used as a proxy for S_{Hmax} at this site.

6 SOURCE MECHANISMS

We compute event focal mechanisms by inverting the observed *P*-wave polarities and relative *P* wave, S_{H} and S_{V} wave amplitudes for the best-fitting double-couple source mechanism. In doing so, we preclude the possibility of non-double-couple sources in our inversion, as might be anticipated during mining-induced seismicity. We do this because the monitoring array consists of only 4 3-C and 3 1-C stations, which limits our ability to robustly constrain non-double-couple events. However, we note that the recovered mechanisms do a reasonable job of fitting the observed polarities, non-double-couple sources do not appear to be necessary to match the majority of our observations.

Of the 305 events, a total of 65 had sufficient signal-to-noise ratios such that *P*-wave polarities could be robustly assigned, and produced reliable and consistent source mechanisms. These strikes, dips and rakes for these events are plotted in Fig. 16. We note three main clusters of event types, representative source mechanisms for which are also plotted.

The most common source mechanism type (numbered 1 in Fig. 16) consists of events with strikes of approximately 50°, high angles of dip and rakes of between 60° and 90°. This source mechanism orientation corresponds to near-vertical planes whose strikes match the strike of the mining face, on which dip-slip movement occurs, with the side of the fault that is towards the mine moving downwards.

A second, less populous source mechanism type (numbered 2 in Fig. 16) shows similar strikes and dips, but with the opposite sense of movement such that the side of the fault towards the mining face moves upwards. Similar event mechanisms—near-vertical failure

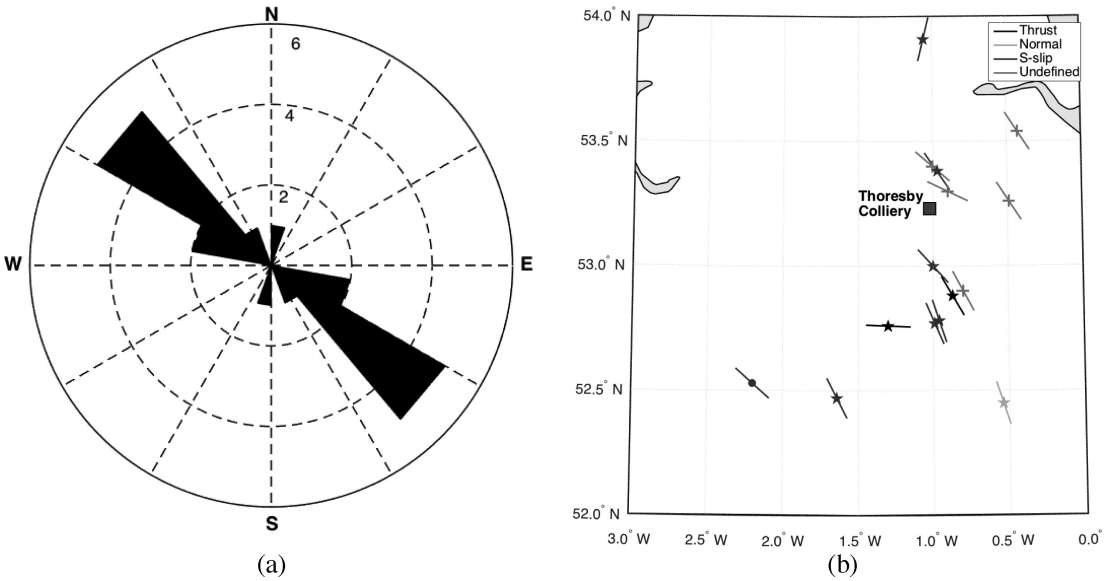

Figure 15. SWS and stress anisotropy. In (a) we plot an angle histogram of the measured SWS fast directions. In (b) we show regional measurements of S_{Hmax} from the World Stress Map database (Heidbach *et al*. 2008): '+' symbols represent borehole breakouts, 'o' symbols represent focal mechanisms, and '⋆' symbols represent hydraulic fracturing data. The Thoresby site is marked by the red square. Measurements are coloured by whether they represent a thrust, normal or strike-slip stress regime (if known).

Table 3. Principal stress orientations and Shape ratio (R) as inverted from event source mechanisms.

Stress	Azimuth	Plunge (down from horizontal)	Shape ratio (R)
σ_1	144°	31°	0.17
σ_2	52°	2°	
σ_3	319°	59°	

planes striking parallel to the mining face with upward and downward dip-slip motion—were observed by Bischoff *et al*. (2010) for longwall mines in the Ruhr Area, Germany, and we share their geomechanical interpretation for these events (Fig. 17). As the coal is mined, the surrounding rock mass will collapse to fill the void. This will result in downward motion of the overlying rock (as per source mechanism type 1), and upward motion of the underlying rock (as per source mechanism type 2) along vertical planes that run parallel to the mining face.

A third type of source mechanism is also observed (numbered 3 in Fig. 16), with thrust-type mechanisms occurring on steeply dipping planes that strike approximately north–south. It is possible that they result from the interaction between mining activities and pre-existing structures in the area, since the N–S orientation of these planes does not match the orientation of any feature in the mine.

Using the source mechanisms for all events, we use the STRESSINVERSE iterative joint inversion algorithm described by Vavrycuk (2014) to estimate the orientations of principal stresses and the shape ratio, R (Gephart & Forsyth 1984):

$$R = \frac{\sigma_1 - \sigma_2}{\sigma_1 - \sigma_3}, \tag{4}$$

where σ_1, σ_2 and σ_3 represent the maximum, intermediate and minimum principal stresses. The results of this inversion are listed in Table 3, and shown in Fig. 18. We note that the resulting maximum horizontal stress is sub-horizontal, with an azimuth of 144°. This is consistent, within error, with the maximum horizontal stress orientation estimated from SWS analysis. This implies that, while the orientations of the slip planes are consistent with the geometry of the mining activities, the resulting deformation is also consistent with the regional *in situ* stress conditions.

7 CONCLUSIONS

In this paper, we characterise the seismicity recorded during longwall mining of the Deep Soft Seam at the Thoresby Colliery, Nottinghamshire, UK. A local monitoring network was installed for 8 months, recording 305 events, with the largest event having a local magnitude of $M_{\mathrm{L}} = 1.7$. Event locations are found to track the advance of the mining faces, with most events being located up to 300 m ahead of the face.

We conclude that these events are 'mining-induced', that is they are directly induced by the mining activity, as opposed to 'mining-tectonic' events, which are caused by static stress transfer producing activation of pre-existing tectonic faults. However, comparison between weekly mining rates and the rates of seismic activity do not show strong correlation. Moreover, the amount of deformation released in the form of seismic events is a small percentage of the overall deformation produced by the mining activities (in other words, most of the deformation is released aseismically).

Event magnitudes do not follow the expected Gutenberg–Richter distribution. Instead, we find that the observed magnitude distribution can be reproduced by assuming that rupture areas follow a TPL distribution, whereby there is a limit to the maximum size of the rupture area. The observed maximum rupture area could correspond to several controlling features around the seam, including the width of the mining face, and the distances to the underlying Parkgate and overlying Top Hard seams, which have already been excavated. Our inference is that the presence of these rubble-filled voids where the excavated seams have been mined out creates a limit to the maximum rupture dimensions.

Event source mechanism analysis shows that most events comprise dip-slip motion along near-vertical planes that strike parallel to the orientation of the mining face. This type of deformation is the expected response to the longwall mining process, and has been

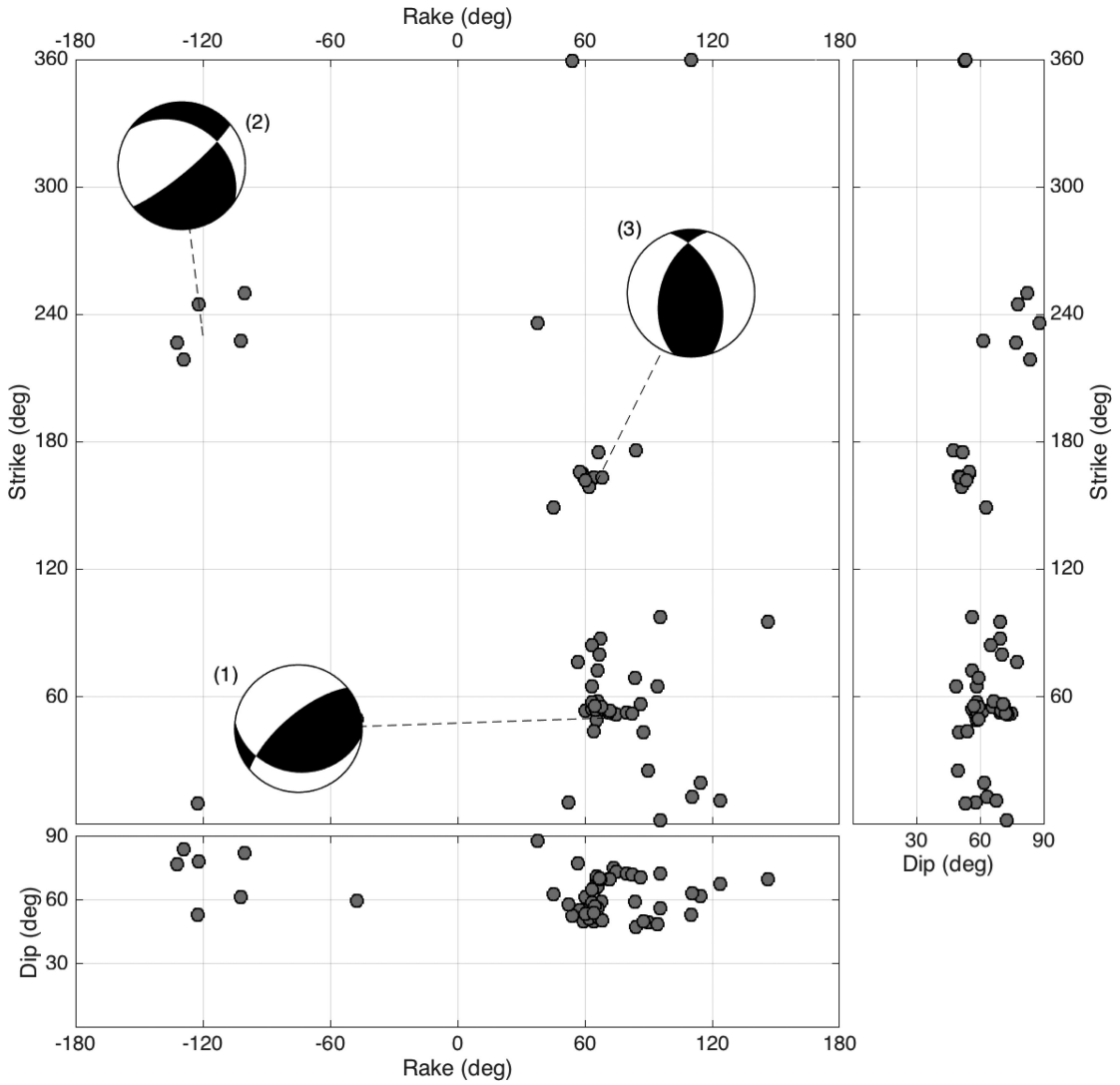

Figure 16. Source mechanisms (strike, dip and rake) for each event for which a reliable mechanism could be obtained. Three main clusters of mechanisms can be identified, representative focal spheres for which are shown. These spheres are upper-hemisphere projections where the compressive quadrants are shaded black.

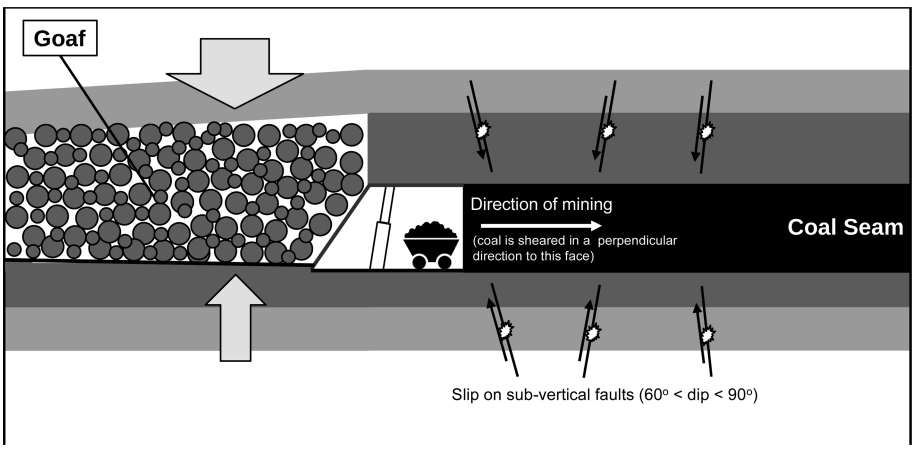

Figure 17. Geomechanical interpretation of the observed source mechanisms. As the surrounding rocks move to fill the void created by mining, dip-slip motion occurs on near-vertical slip planes oriented parallel to the mining face. Adapted from Bischoff *et al*. (2010).

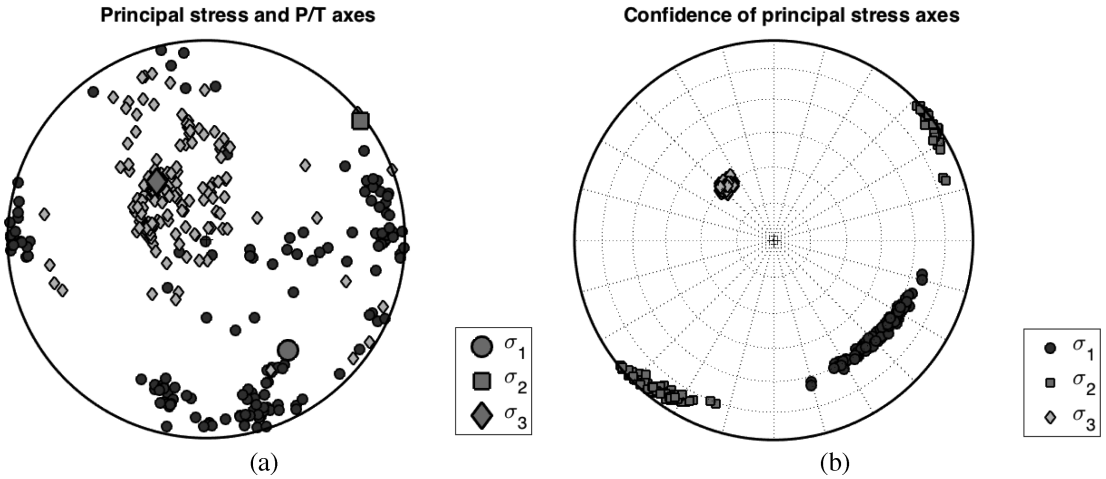

Figure 18. Stress tensor inversion results using the STRESSINVERSE algorithm (Vavrycuk 2014). In (a) we show a lower hemisphere projection of the P (dark grey ◯) and T (light grey ◇) axes for every event, with the overall estimate for the σ_1, σ_2 and σ_3 axes marked by a large ◯, □ and ◇, respectively. In (b) we show confidence limits for the principle stress axes, assuming $\pm 15^\circ$ error in source mechanism orientations.

observed at other longwall mining sites. The observed source mechanisms are also consistent with the orientation of *in situ* regional stresses as inferred from SWS analysis.

ACKNOWLEDGEMENTS

JPV and JMK are funded by the BGS/University of Bristol Strategic Partnership in Applied Geophysics. This work was performed as part of the Bristol University Microseismicity Project (BUMPS).

REFERENCES

Abercrombie, R.E., 1995. Earthquake source scaling relationships from −1 to 5 M_L using seismograms recorded at 2.5-km depth, *J. geophys. Res.,* **100,** 24 015–24 036.

Allen, R., 1982. Automatic phase pickers: their present use and future prospects, *Bull. seism. Soc. Am.,* **72,** S225–S242.

Bischoff, M., Cete, A., Fritschen, R. & Meier, T., 2010. Coal mining induced seismicity in the Ruhr area, Germany, *Pure appl. Geophys.,* **167,** 63–75.

Bishop, I., Styles, P. & Allen, M., 1993. Mining-induced seismicity in the Nottinghamshire coalfield, *Quart. J. Eng. Geol. Hydrogeol.,* **26,** 253–279.

Boness, N.L. & Zoback, M.D., 2006. Mapping stress and structurally controlled crustal shear velocity anisotropy in California, *Geology,* **34,** 825–828.

Bonnet, E., Bour, O., Odling, N.E., Davy, P., Main, I., Cowie, P. & Berkowitz, B., 2001. Scaling of fracture systems in geological media, *Rev. Geophys.,* **39,** 347–383.

Brune, J.N., 1970. Tectonic stress and the spectra of seismic shear waves from earthquakes, *J. geophys. Res.,* **75,** 4997–5009.

Burroughs, S.M., 2002. The upper-truncated power law applied to earthquake cumulative frequency-magnitude distributions: evidence for a time-independent scaling parameter, *Bull. seism. Soc. Am.,* **92,** 2983–2993.

Burroughs, S.M. & Tebbens, S.F., 2001. Upper-truncated power laws in natural systems, *Pure appl. geophys.,* **158,** 741–757.

Butcher, A., Luckett, R., Verdon, J.P., Kendall, J.-M., Baptie, B. & Wookey, J., 2017. Local magnitude discrepancies for near-event receivers: implications for the U.K. traffic-light scheme, *Bull. seism. Soc. Am.,* **107**(2), 532–541.

Cook, N.G.W., 1976. Seismicity associated with mining, *Eng. Geol.,* **10,** 99–122.

Crampin, S. & Peacock, S., 2008. A review of the current understanding of seismic shear-wave splitting in the Earth's crust and common fallacies in interpretation, *Wave Motion,* **45,** 675–722.

Edwards, W.N., 1967. Geology of the country around Ollerton. Memoirs of the Geological Survey of Great Britain, Her Majesty's Stationery Office. Available at: http://pubs.bgs.ac.uk/publications.html?pubID=B01568.

Gephart, J.W. & Forsyth, D.W., 1984. An improved method for determining the regional stress tensor using earthquake focal mechanism data: application to the San Fernando earthquake sequence, *J. geophys. Res.,* **89,** 9305–9320.

Gibowicz, S.J., Harjes, H.-J. & Schäfer, M., 1990. Source parameters of seismic events at Heinrich Robert Mine, Ruhr Basin, Federal Republic of Germany: evidence for nondouble-couple events, *Bull. seism. Soc. Am.,* **80,** 88–109.

Gutenberg, B. & Richter, C.F., 1944. Frequency of earthquakes in California, *Bull. seism. Soc. Am.,* **34,** 185–188.

Hallo, M., Oprsal, I., Eisner, L. & Ali, M.Y., 2014. Prediction of magnitude of the largest potentially induced seismic event, *J. Seismol.,* **18,** 421–431.

Heidbach, O., Tingay, M., Barth, A., Reinecker, J., Kurfeß, D. & Müller, B., 2008. The World Stress Map Database Release 2008.

Hudyma, M., Potvin, Y. & Allison, D., 2008. Seismic monitoring of the Northparkes Lift 2 block cave—Part 2. Production caving, *J. S. Afr. Inst. Min. Metall.,* **108,** 421–430.

Kanamori, H. & Brodsky, E.E., 2004. The physics of earthquakes, *Rep. Prog. Phys.,* **67,** 1429–1496.

Kwiatek, G., Plenkers, K. & Dresen, G., JAGUARS Research Group, 2011. Source parameters of picoseismicity recorded at Mponeng Deep Gold Mine, South Africa: implications for scaling relations, *Bull. seism. Soc. Am.,* **101,** 2592–2608.

Maxwell, S.C., Shemeta, J., Campbell, E. & Quirk, D., 2008. Microseismic deformation rate monitoring, in *Proceedings of the SPE Annual Technical Conference,* Denver, SPE 116596.

McGarr, A., 1976. Seismic moments and volume changes, *J. geophys. Res.,* **81,** 1487–1494.

McGarr, A., 2014. Maximum magnitude earthquakes induced by fluid injection, *J. geophys. Res.,* **119,** 1008–1019.

Ottemoller, L. & Sargeant, S., 2013. A local magnitude scale M_L for the United Kingdom, *Bull. seism. Soc. Am.,* **103,** 2884–2893.

Pacheco, J.F., Scholz, C.H. & Sykes, L.R., 1992. Changes in frequency-size relationship from small to large earthquakes, *Nature,* **355,** 71–73.

Podvin, P. & Lecomte, I., 1991. Finite difference computation of traveltimes in very contrasted velocity models: a massively parallel approach and its associated tools, *Geophys. J. Int.,* **105,** 271–284.

Redmayne, D.W., 1988. Mining induced seismicity in UK coalfields identified on the BGS national seismograph network, in *Engineering Geology of Underground Movements,* eds Bell, F.G., Culshaw, M.G., Cripps, J.C. & Lovell, M.A., pp. 405–413, Geological Society Engineering Geology Special Publication no. 5.

Richter, C.F., 1958. *Elementary Seismology,* Freeman and Co.

Sambridge, M., 1999. Geophysical inversion with a neighbourhood algorithm—I. Searching a parameter space, *Geophys. J. Int.,* **138,** 479–494.

Scholz, C.H. & Contreras, J.C., 1998. Mechanics of continental rift architecture, *Geology,* **26,** 967–970.

Sen, A.T., Cesca, S., Bischoff, M., Meier, T. & Dahm, T., 2013. Automated full moment tensor inversion of coal mining-induced seismicity, *Geophys. J. Int.,* **195,** 1267–1281.

Shapiro, S.A., Krüger, O.S. & Dinske, C., 2013. Probability of inducing given-magnitude earthquakes by perturbing finite volumes of rocks, *J. geophys. Res.,* **118,** 3557–3575.

Stec, K., 2007. Characteristics of seismic activity of the Upper Silesian Coal Basin in Poland, *Geophys. J. Int.,* **168,** 757–768.

Stork, A.L., Verdon, J.P. & Kendall, J.-M., 2014. The robustness of seismic moment and magnitudes estimated using spectral analysis, *Geophys. Prospect.,* **62,** 862–878.

Teanby, N.A., 2004. Automation of shear-wave splitting measurements using cluster analysis, *Bull. seism. Soc. Am.,* **94,** 453–463.

Turvill, W., 2014. Welcome to Britain's earthquake capital: Sleepy Nottinghamshire town has been hit by 36 tremoers in just 50 days – and geologists say mining is to blame, *The Daily Mail*, Available at: http://www.dailymail.co.uk/news/article-2548146/Welcome-Britains-EARTHQUAKE-capital-Sleepy-Nottinghamshire-town-hit-36-tremors-just-50-days-geologists-say-mining-blame.html, last accessed 21 January 2017.

UK Coal Authority Mine Abandonment Plans, 2017. Mine Abandonment Plans are available upon application to the UK Coal Authority. Available at: https://www.gov.uk/guidance/coal-mining-records-data-deeds-and-documents.

Vavrycuk, V., 2014. Iterative joint inversion for stress and fault orientations from focal mechanisms, *Geophys. J. Int.,* **199,** 69–77.

Wesnousky, S.G., Scholz, C.H., Shimazaki, K. & Matsuda, T., 1983. Earthquake frequency distribution and the mechanics of faulting, *J. geophys. Res.,* **88,** 9331–9340.

Wilson, M.P., Davies, R.J., Foulger, G.R., Julian, B.R., Styles, P., Gluyas, J.G. & Almond, S., 2015. Anthropogenic earthquakes in the UK: a national baseline prior to shale exploitation, *Mar. Petrol. Geol.,* **68,** 1–17.

Wuestefeld, A., Al-Harrasi, O., Verdon, J.P., Wookey, J. & Kendall, J.M., 2010. A strategy for automated analysis of passive microseismic data to image seismic anisotropy and fracture characteristics, *Geophys. Prospect.,* **58,** 755–773.

Wuestefeld, A., Kendall, J.M., Verdon, J.P. & Van As, A., 2011. *In situ* monitoring of rock fracturing using shear wave splitting analysis: an example from a mining setting, *Geophys. J. Int.,* **187,** 848–860.

Younger, P.L., 2016. How can we be sure fracking will not pollute aquifers? Lessons from a major longwall coal mining analogue (Selby, Yorkshire, UK), *Earth Environ. Sci. Trans. R. Soc. Edinburgh,* **106,** 89–113.